

Precipitated Iodine Cathode Enabled by Trifluoromethanesulfonate Oxidation for Cathode/Electrolyte Mutualistic Aqueous Zn–I Batteries

Kaiqiang Zhang, Qianchuan Yu, Jingjie Sun, Zuoxiu Tie, and Zhong Jin*

Aqueous Zn–I batteries hold great potential for high-safety and sustainable energy storage. However, the iodide shuttling effect and the hydrogen evolution reaction that occur in the aqueous electrolyte remain the main obstacles for their further development. Herein, the design of a cathode/electrolyte mutualistic aqueous (CEMA) Zn–I battery based on the inherent oxidation ability of aqueous trifluoromethanesulfonate ((OTf)[−]) electrolyte toward triiodide species is presented. This results in the formation of iodine sediment particles assembled by fine iodine nanocrystals (≈ 10 nm). An iodine host cathode with high areal iodine loading is realized via a spontaneous absorption process that enriched redox-active iodine and iodide species from aqueous electrolyte onto nanoporous carbon based current collector. By tuning iodide redox process and suppressing competitive hydrogen evolution reaction, the assembled CEMA Zn–I batteries demonstrate a remarkable capacity retention of 76.9% over 1000 cycles at 0.5 mA cm^{-2} . Moreover, they exhibit a notable rate capability, with a capacity retention of 74.6% when the current density is increased from 0.5 to 5.0 mA cm^{-2} . This study demonstrates the feasibility of using the oxidation effect to repel redox-active species from the electrolyte to the cathode, paving a new avenue for high-performance aqueous Zn–I batteries.

1. Introduction

Aqueous Zn–ion batteries have gained considerable attention due to their unique advantages, including intrinsic safety, environmental benignity, and easy operation in air.^[1–5] Among various Zn–ion battery systems,^[6–9] such as Zn–halogen,^[10–12] Zn–air,^[13,14] Zn–S,^[15,16] Zn–metal oxide batteries,^[17,18] the aqueous Zn–I battery employing a typical conversion-type redox

chemistry of an I_2/I^- couple is considered a promising candidate for scalable applications due to its high energy density and affordable costs.^[19,20] However, the polyiodide shuttling effect during battery operation remains an obstacle to commercialization progress. To mitigate the polyiodide shuttling effect, extensive research efforts have been carried out, which mainly involve exploring various functional materials, such as nanoporous carbons, metal-containing compounds with catalytic activity, sieving membranes, and solid-state electrolytes.^[21–24] These materials are able to absorb, electrostatically repel, and sieve iodide species, thereby improving the cycling ability, coulombic efficiency, and electrochemical kinetics.^[25–28] However, this approach inevitably drags the improvement of overall energy density. In addition, hydrogen evolution reaction (HER) occurs in aqueous electrolyte when the battery voltage exceeds its critical potential.^[29–32] The undesired HER in aqueous Zn–ion batteries, including Zn–I system, often leads to the drawbacks, including the formation of

flammable H_2 , battery swelling, and low charge storage efficiency.^[33–38] Therefore, it is crucial to have a comprehensive strategy to inhibit the polyiodide shuttling and the HER without sacrificing energy density. A promising solution would be to develop an aqueous electrolyte that spontaneously expels iodide species, mitigates polyiodide diffusion, and suppresses the interactions of redox species/electrolyte. However, such consideration has rarely been addressed in previous studies of aqueous Zn–I batteries.

Herein, we present a self-expelling strategy toward iodide species by harnessing the inherent oxidation effect of trifluoromethanesulfonate ((OTf)[−]) in $\text{Zn}(\text{OTf})_2$ aqueous electrolyte. Upon the addition of I_3^- species in the $\text{Zn}(\text{OTf})_2$ aqueous electrolyte, (OTf)[−] induced the formation of iodine sediment particles, leading to a mutualistic mixture of iodine sediment particles and aqueous electrolyte. Based on this mixture, we developed a cathode/electrolyte mutualistic aqueous (CEMA) Zn–I battery. During battery assembly, the iodine cathode and aqueous electrolyte were simultaneously formed through a facile in situ filtering process, where the iodine and iodide species were retained by the carbon host cathode while the aqueous electrolyte further penetrated until reaching the metallic Zn anode. By tuning the

K. Zhang, Q. Yu, J. Sun, Z. Tie, Z. Jin
State Key Laboratory of Coordination Chemistry
MOE Key Laboratory of Mesoscopic Chemistry
MOE Key Laboratory of High Performance Polymer Materials and Technology
Jiangsu Key Laboratory of Advanced Organic Materials
School of Chemistry and Chemical Engineering
Nanjing University
Nanjing, Jiangsu 210023, P. R. China
E-mail: zhongjin@nju.edu.cn

The ORCID identification number(s) for the author(s) of this article can be found under <https://doi.org/10.1002/adma.202309838>

DOI: 10.1002/adma.202309838

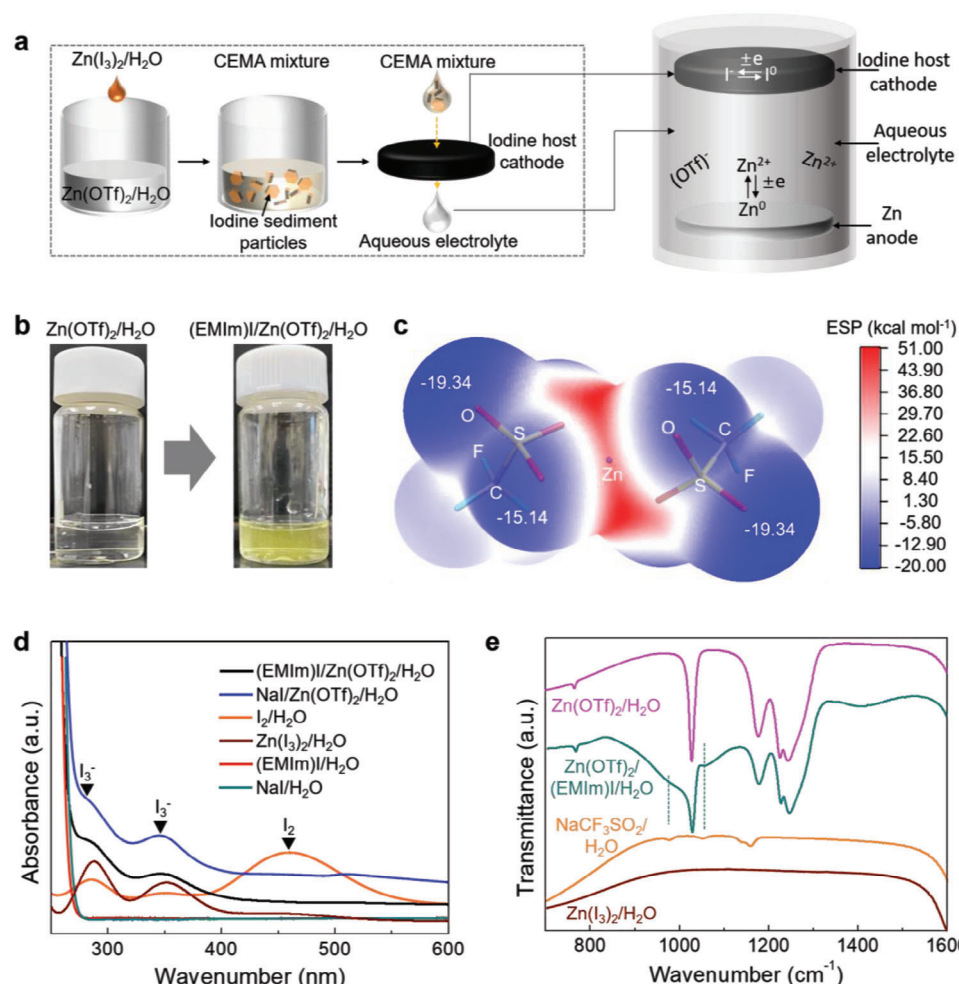


Figure 1. Schematic illustration of CEMA Zn-I batteries and characterizations of oxidation effects of $(\text{OTf})^-$ on iodide species. a) Schematic configuration of the CEMA Zn-I batteries. b) Oxidation effects of $(\text{OTf})^-$ on I^- species. c) Theoretical calculation of MESP for $\text{Zn}(\text{OTf})_2$. d) UV-vis spectra of $(\text{EMIm})\text{I}/\text{Zn}(\text{OTf})_2$, $\text{NaI}/\text{Zn}(\text{OTf})_2$, I_2 , $\text{Zn}(\text{I}_3)_2$, $(\text{EMIm})\text{I}$, and NaI aqueous solutions. e) FTIR spectra of $\text{Zn}(\text{OTf})_2$, $\text{Zn}(\text{OTf})_2/(\text{EMIm})\text{I}$, NaCF_3SO_2 , and $\text{Zn}(\text{I}_3)_2$ aqueous solutions.

I_2/I^- ratios and I_3^- concentrations, the iodide oxidation reaction was efficiently facilitated and the unwanted HER suppressed. The fabricated CEMA Zn-I batteries exhibited high rate performance, with a capacity retention ratio of 74.6% as the operation current density increased from 0.5 to 5.0 mA cm^{-2} . Long-term cycling tests revealed efficient control over the polyiodide shuttling effect, benefitting from the oxidation effects of $(\text{OTf})^-$ on iodide species. The optimized pouch-type CEMA Zn-I batteries showed no distinct swelling after repeated galvanostatic charge/discharge tests, suggesting efficient inhibition of the HER. Our work provides proof of concept for the repelling effect of electrolyte on iodide species owing to its inherent oxidation ability, promoting the development of advanced aqueous Zn-I batteries.

2. Results and Discussion

2.1. Oxidative Effect of $(\text{OTf})^-$ on Iodide Species

The CEMA Zn-I battery was fabricated using a Zn anode, an aqueous electrolyte containing iodine sediment particles, and an

iodine host cathode, as illustrated in **Figure 1a** and detailed in the Experimental Section. Notably, the iodine sediment particles-containing aqueous electrolyte serves as a source of redox-active iodide species, as well as an aqueous electrolyte for constructing the Zn-I battery. The oxidation effect of $(\text{OTf})^-$ on iodide species was experimentally demonstrated by adding ZnI_2 , $(\text{EMIm})\text{I}$, or NaI chemical reagents in 3 M $\text{Zn}(\text{OTf})_2$ aqueous solutions, respectively. The transparent $\text{Zn}(\text{OTf})_2$ aqueous solutions turned yellow immediately (Figure 1b and Figure S1a,c, Supporting Information), confirming the occurrence of iodide oxidation. In contrast, no such color change was observed in the control experiment using a 3 M ZnCl_2 aqueous solution, even after adding the iodide reagent (Figure S1b, Supporting Information), indicating the absence of iodide oxidation reactions. These results suggest that the $(\text{OTf})^-$ anions are responsible for the iodide oxidation reactions. However, this oxidation behavior was not observed for Br^- species (Figure S1d,e, Supporting Information), likely owing to their lower oxidability. To gain a comprehensive understanding of the oxidation behavior of $(\text{OTf})^-$ on iodide species, we conducted additional theoretical calculations of

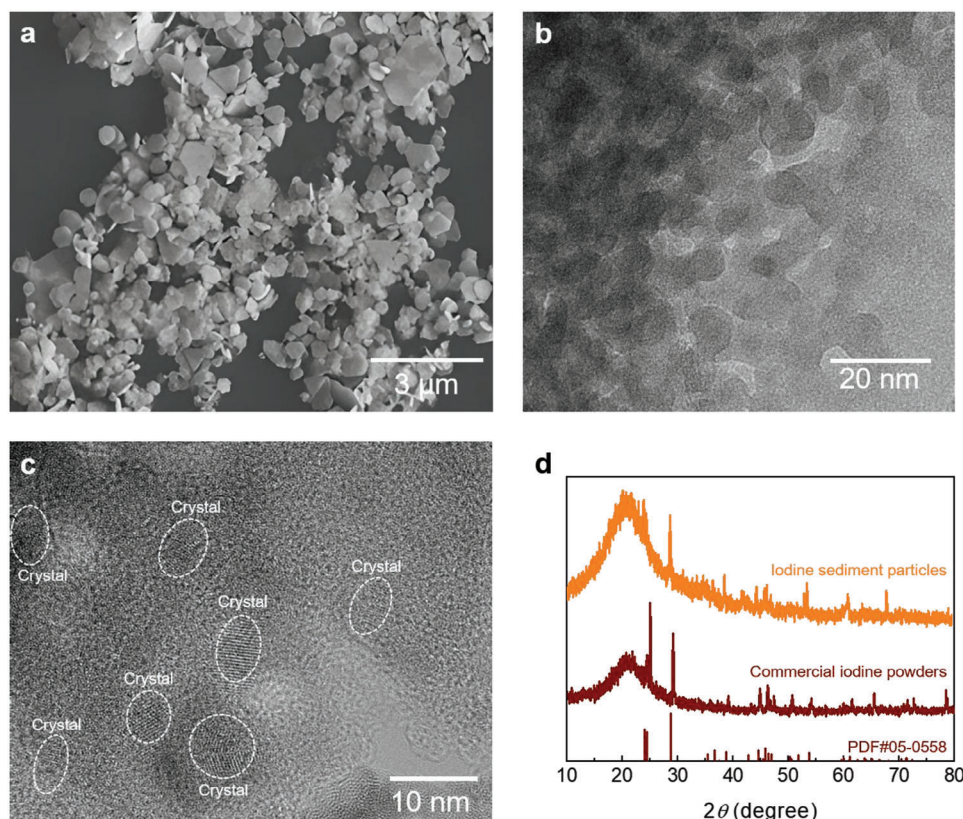


Figure 2. Characterizations of the iodine sediment particles formed by the oxidation effect of $(\text{OTf})^-$. a) SEM, b) TEM, and c) HRTEM images of iodine sediment particles. d) XRD spectra of iodine sediment particles and commercial iodine powders.

molecular electrostatic potential (MESP) for $\text{Zn}(\text{OTf})_2$. As shown in Figure 1c, the result indicates that the $-\text{SO}_3$ moiety displays a lower MESP of $-19.34 \text{ kcal mol}^{-1}$ compared to that of the $-\text{CF}_3$ moiety ($-15.14 \text{ kcal mol}^{-1}$). These theoretical calculation results provide a more comprehensive understanding for the oxidation property of $(\text{OTf})^-$ species.

The oxidation product of iodide species by $(\text{OTf})^-$ was characterized using ultraviolet–visible (UV–vis) spectroscopy, as depicted in Figure 1d. The presence of UV–vis absorption peaks at 288 and 345 nm confirmed the formation of triiodide (I_3^-) anions, consistent with the $\text{Zn}(\text{I}_3)_2$ control sample. However, in the control experiment using NaI and $(\text{EMIm})\text{I}$ aqueous solutions, these UV–vis absorption peaks were absent (Figure 1d). Furthermore, the reductant product of $(\text{OTf})^-$ by iodide ions was analyzed using Fourier transform infrared (FTIR) spectroscopy. The FTIR spectrum of the $\text{Zn}(\text{OTf})_2$ aqueous solution after oxidation reaction showed locally emerging FTIR transmittance peaks at 975, 1060, and 1410 cm^{-1} , while other peaks remained consistent with the standard sample (Figure 1e). The absence of these characteristic peaks in the FTIR spectrum of the standard $\text{Zn}(\text{I}_3)_2$ aqueous solution excludes the possibility of their origin in the formed triiodide product. These experimental results suggested a change in binding association within $(\text{OTf})^-$. The electron paramagnetic resonance (EPR) analysis data (Figure S2, Supporting Information) further indicated a straightforward oxidation mechanism.

Drawing upon the distinctive structural characteristics of the $(\text{OTf})^-$ anion, which features unsaturated $\text{S}=\text{O}$ double bonds with inherent oxidability potential, we anticipate that these double bonds could undergo alteration during the oxidation reaction with iodide species. A detailed analysis of the FTIR spectra data (Figure 1e) for the reduced $(\text{OTf})^-$ supports the inference that the $(\text{OTf})^-$ anions could possibly be reduced to trifluoromethanesulfinate (CF_3SO_2^-) by the action of iodide species, consistent with the observation that $\text{S}=\text{O}$ bond vibrations typically manifest in the spectral range of $\approx 1000, 1100, 1200$, and 1400 cm^{-1} .^[39–42]

2.2. Oxidation Effect of $(\text{OTf})^-$ on Triiodide Species

In light of the oxidative effect of $(\text{OTf})^-$ on iodide species, we conducted further studies to investigate its impact on triiodide species (I_3^-). In the first step, a $\text{Zn}(\text{I}_3)_2$ aqueous solution was prepared, which was subsequently injected into a 3 M $\text{Zn}(\text{OTf})_2$ aqueous solution, as detailed in the Experimental Section. Upon injecting the prepared $\text{Zn}(\text{I}_3)_2$ aqueous solution, we immediately observed the formation of iodine sediment particles, as demonstrated in Video S1 (Supporting Information). The precipitation process was expedited by the limited water solubility of iodine. Scanning electron microscopy (SEM) analysis of iodine sediment particles revealed the plate-shaped morphology with distinct sizes, as presented in Figure 2a. Subsequent transmittance

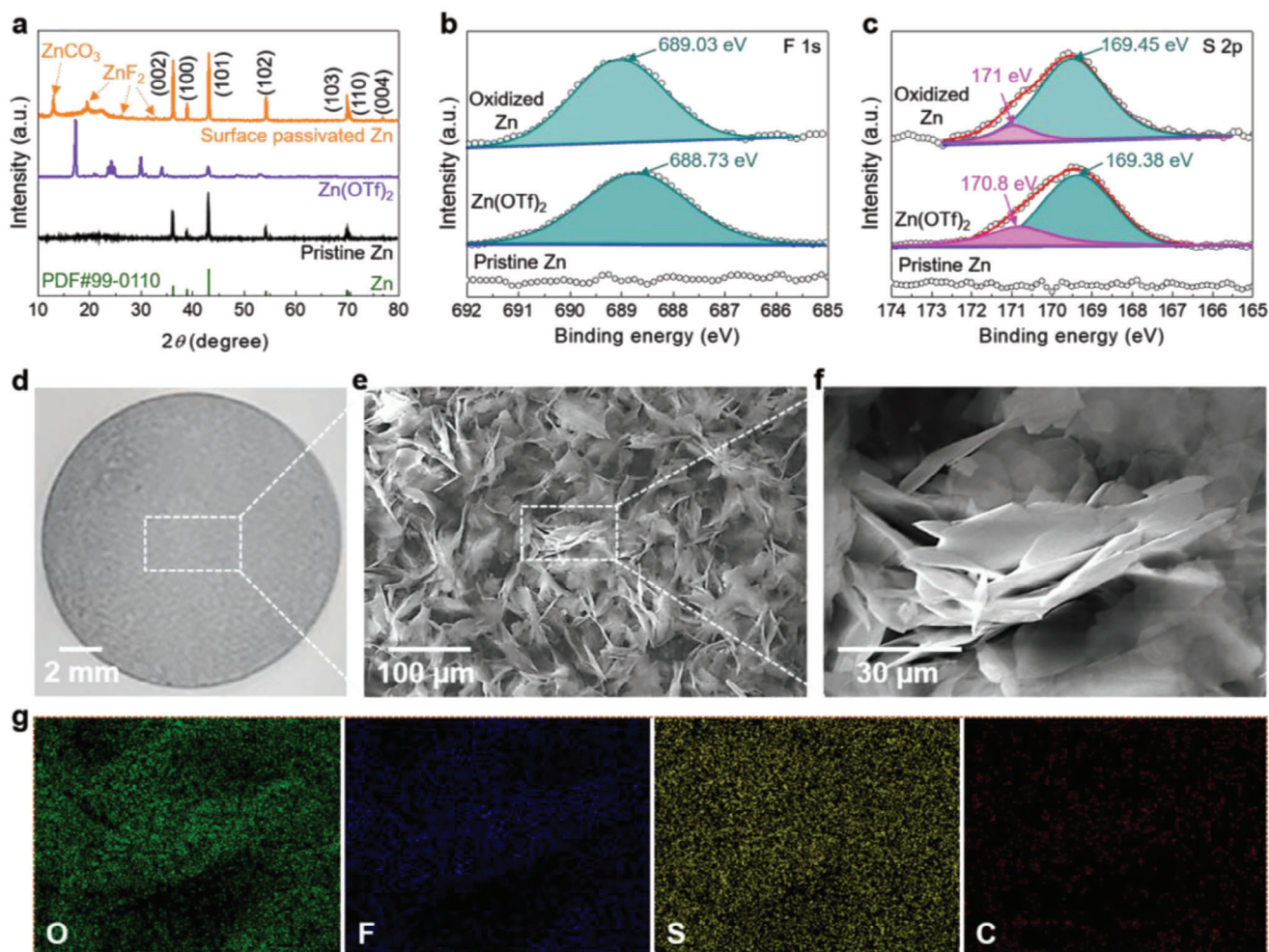


Figure 3. Characterizations of surface passivated Zn foil treated by (OTf)[−]. a) XRD spectra of surface passivated Zn foil, Zn(OTf)₂, and pristine Zn foil. b,c) Deconvoluted XPS spectra at F 1s and S 2p regions of surface passivated Zn foil, Zn(OTf)₂, and pristine Zn foil. d) Optical and e,f) SEM images of surface passivated Zn foil. g) EDX elemental mappings corresponding to the region in (f).

electron microscopy (TEM) and high-resolution TEM (HRTEM) observations showed a nanoporous structure assembled by tiny iodine nanocrystals with the size of ≈ 10 nm (Figure 2b,c). This is an unknown phenomenon in prior studies conducted on redox-active iodine electrodes.^[43–45] X-ray diffraction (XRD) analysis confirmed that the sediment particles were composed of iodine species, as demonstrated by the characteristic peaks at 24.5° , 28.7° , 44.4° , and 45.8° in Figure 2d. Additional experiments on dissolution of the iodine sediment particles were carried out by dissolving them in a CCl₄ organic solvent. As a result, a purple solution was obtained after particle dissolution, which is comparable to I₂/CCl₄ solution, as shown in Figure S3 (Supporting Information). Conversely, chemical reagents of ZnI₂ and Zn(OTf)₂ were found to be insoluble in the CCl₄ solvent (Figure S3a–d, Supporting Information). Furthermore, upon substituting the (OTf)[−] solution with (SO₄)^{2−}, it became apparent that iodine sediment particles formed within the opaque mixture, as opposed to the transparent solution (Figure S3e,f, Supporting Information). Based on these experimental findings, we could infer that (OTf)[−] exerted an oxidative effect on triiodide species, resulting

in the production of additional iodine products. The appearance of identical peaks at ≈ 975 , 1060 , and 1410 cm^{−1} in the FTIR spectra of Zn(OTf)₂ aqueous solutions after triiodide oxidation reactions indicates the alteration in the association state of (OTf)[−] ions (Figure S4, Supporting Information).

2.3. Surface Passivation Effect of (OTf)[−] on Metallic Zn

The inherent reductive property of Zn metal necessitates an investigation of the surface passivation effect of (OTf)[−] on Zn metal anode. To accomplish this, Zn foil was immersed in a 3 M Zn(OTf)₂ aqueous solution to initiate the surface reaction of Zn by (OTf)[−], as detailed in the Experimental Section. XRD analysis of the surface-passivated Zn foil revealed distinct peak signals at 13.0° , 19.6° , and 26.5° , indicative of the decomposition of (OTf)[−] anions on the Zn metal surface (Figure 3a). These findings well align with prior research and are consistent with previous reports on the subject.^[29,46,47] The emergence of these XRD signals in the soaked Zn foil compared to the pristine Zn foil and

$\text{Zn}(\text{OTf})_2$ suggests that the underlying surface reactions occurred during the immersion of metallic Zn in the $\text{Zn}(\text{OTf})_2$ aqueous solution achieves the formation of an interfacial passivation layer. The surficial chemical compositions of both surface passivated and pristine Zn foils were performed using X-ray photoelectron spectroscopy (XPS). The deconvoluted F 1s XPS spectra exhibited a newly emerged peak at 689.03 eV, suggesting the existence of F species due to the surface reaction of Zn metal, which is absent for the pristine Zn foil. The association environment of F in surface passivation layer differs from that in $\text{Zn}(\text{OTf})_2$, as demonstrated by the shift in binding energy by 0.3 eV (Figure 3b). In addition, S was also found to participate in the formation of the surface passivation layer on Zn foil, as demonstrated by the binding peaks at 169.45 and 171 eV in the deconvoluted S 2p XPS spectra (Figure 3c). In contrast, these XPS signals were absent for the pristine Zn foil. Surface morphologies observed using SEM revealed a rougher Zn surface with deposited nanoplates (Figure 3d,f). Overall, these results demonstrate the surface reaction of Zn metal with $(\text{OTf})^-$ anions, leading to the formation of a surface passivation layer. The surface passivated Zn surface was further subjected to elemental analysis using energy-dispersive X-ray (EDX) spectroscopy. Elemental mappings revealed the presence of F, S, and O elements in the interfacial layer, as shown in Figure 3g and Figure S5 (Supporting Information). It is noteworthy that the intensity of O element in the surface passivation layer was considerably higher than that in pristine Zn, as confirmed in Figure S5 (Supporting Information). This indicates that intense oxidation reactions took place on the Zn foils. The emergence of elemental peaks for F and S elements in the surface passivation layer of Zn, compared with the pristine Zn foil, further suggests the surface passivation reactions of Zn mediated by $(\text{OTf})^-$. The FTIR analysis of $\text{Zn}(\text{OTf})_2$ aqueous solution after the surface passivation of Zn foil showed no emerged peaks (Figure S6, Supporting Information). This suggests that the surface functionalization of Zn by $(\text{OTf})^-$ only involves interfacial $(\text{OTf})^-$, while the others maintain consistent ionic associations with the fresh sample. Furthermore, this observation implies that the generated oxidized layer exhibits both ionic conductive and electronic insulation properties, contributing to the significant mitigation of the HER during battery operation.

2.4. Promoting Iodide Redox and Suppressing HER Processes

During battery operation, there is probably a competitive interplay between the iodide redox and HER processes within the CEMA Zn–I batteries, potentially accompanied by the polyiodide shuttling effect (Figure S7, Supporting Information). This competitive process was investigated by analyzing the coulombic efficiency parameter during battery cycling. At relatively high I_2/I^- ratios and lower concentrations of I_3^- , the HER processes could be efficiently suppressed, thereby promoting the iodide redox reactions (Figures S8 and S9, Supporting Information). We proposed that higher ratios of I_2/I^- and lower concentrations of I_3^- led to less retained/unoxidized iodide and triiodide species, which inhibited the ionizing effect between iodide/triiodide species and H_2O molecules, thereby suppressing the HER and facilitating the iodide redox process. In addition, by increasing the concentration of I_3^- and adjusting the charge cut-

off voltages, we can modulate the charge-storage capacity while maintaining high coulombic efficiency. These findings suggest that careful control of the electrolyte composition and operating conditions can enhance the performance of CEMA Zn–I batteries.

Moreover, the insulating characteristics of the oxidation layer on the Zn anode offer great advantages in alleviating the HER on the Zn/aqueous electrolyte interface. In the typical charging process, water molecules associated with hydrated Zn^{2+} ions were displaced, enabling Zn^{2+} ions to actively engage in the reduction reaction. This concept has been robustly demonstrated in various Zn surface modification strategies aimed at curbing dendrite growth and suppressing the HER.^[48,49]

2.5. Electrochemical Studies of CEMA Zn–I Batteries

The electrochemical performance of CEMA Zn–I batteries was systematically investigated at room temperature at various conditions. First, we examined the cyclic voltammetry (CV) curves of CEMA Zn–I batteries with various I_3^- concentrations and I_2/I^- ratios and found that the discharge reaction of CEMA Zn–I batteries involved a two-step iodide redox process ($\text{I}_2 \rightarrow \text{I}_3^- \rightarrow \text{I}^-$) as demonstrated by the bifurcate discharge peaks in the CV curves (Figure S10, Supporting Information).^[50] The CV curves collected from 3–1/1 (i.e., an I_2 concentration of 3 M and an I_2/I^- ratio of 1/1) CEMA Zn–I batteries with an iodide areal loading amount of 0.69 mg cm⁻² at 100 mV s⁻¹ exhibit a pair of redox peaks with a voltage hysteresis of 0.2 V, as illustrated in Figure 4a. These experiment results demonstrate the suppression of the HER and suggest the existence of an optimal operating condition for each CEMA scenario within the context of this innovative CEMA Zn–I battery. To provide a comprehensive and scientifically grounded understanding of this battery design concept, we have included modified electrochemical performance data for Zn–I batteries with a range of CEMA scenarios. The rate performance of 3–1/1 CEMA Zn–I batteries was evaluated at various current densities (0.5, 1.0, 2.0, 3.0, 4.0, and 5.0 mA cm⁻²), demonstrating a capacity retention ratio of 74.6% (with the specific capacity attenuated from 130 to 97 mAh g⁻¹, or from 0.09 to 0.07 mAh cm⁻² in area) after a tenfold increase in current densities, as shown in Figure 4b. The voltage profiles of the CEMA Zn–I batteries at each current density exhibited a single voltage plateau, as indicated in Figure 4c. To account for the coulombic efficiencies higher than 100% at lower current densities, we, in part, attribute this outcome to the influence of the internal electric field. Typically, during battery charging, an electric field is established in the direction towards the anode. This electric field facilitates the migration of negatively charged $(\text{OTf})^-$ anions towards the cathode side. Conversely, the direction of this electric field reverses during battery discharging. Considering the potential occurrence of chemical reactions between Zn anode and $(\text{OTf})^-$ anions, the discharging operation is more conducive to promoting this process compared to the charging process, resulting in a larger recorded charge quantity. Long-term cycling tests were conducted for the CEMA Zn–I batteries with various I_3^- concentrations (1–1/1, 2–1/1, and 10–1/1 corresponding to iodide areal loading amounts of 0.23, 0.46, and 2.3 mg cm⁻², respectively) at different current densities. The 1–1/1 CEMA

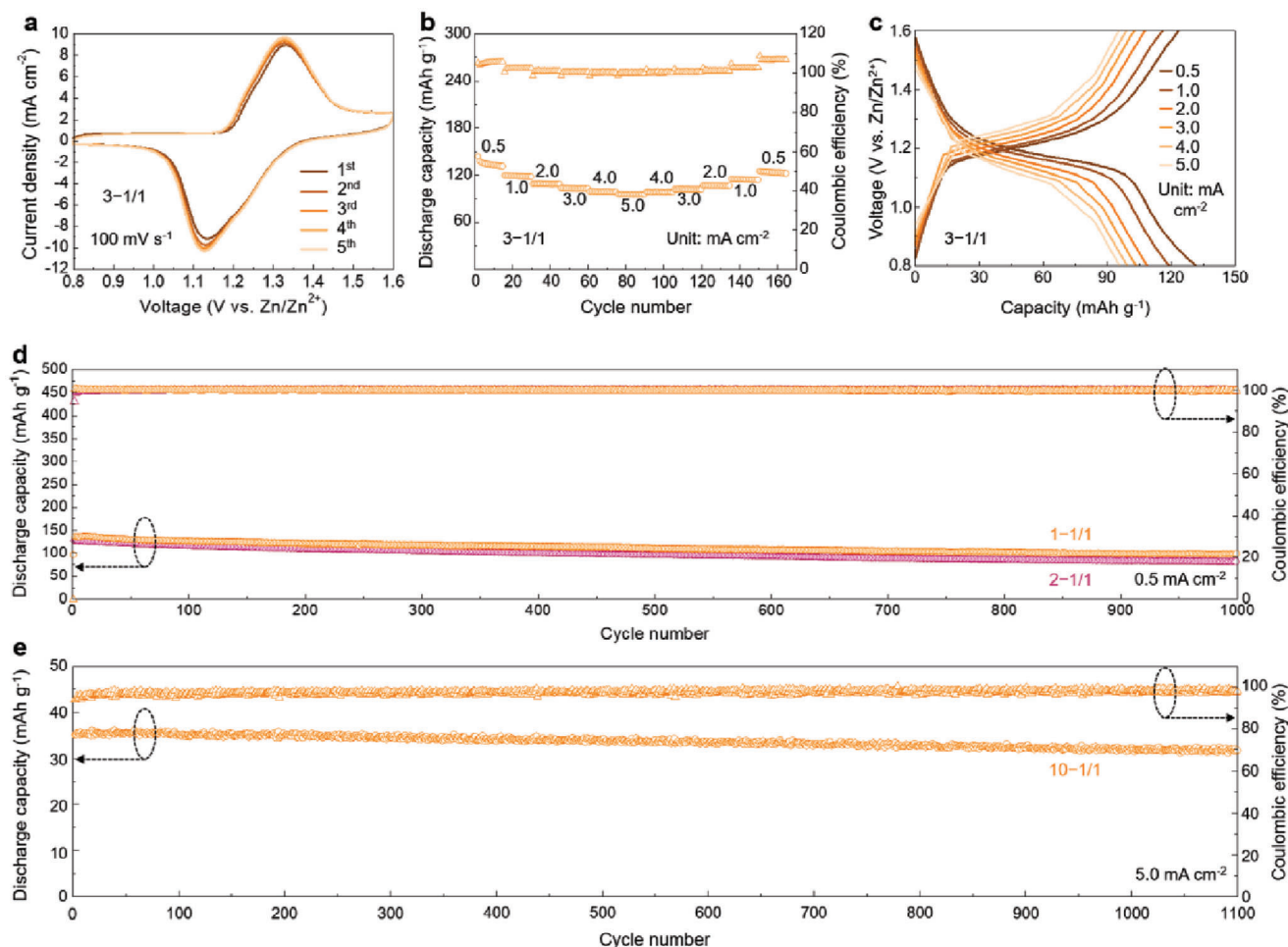


Figure 4. Electrochemical performance of the CEMA Zn-I batteries. a) CV curves, b) rate performance, and c) voltage profiles of the 3-1/1 CEMA Zn-I batteries. Long-term cycling tests of the d) 1-1/1, 2-1/1 and e) 10-1/1 CEMA Zn-I batteries at 0.5 and 5.0 mA cm⁻², respectively.

Zn-I batteries demonstrated stable cycling abilities, exhibiting a capacity retention ratio of 76.9% (with the specific capacity attenuated from 141 to 112 mAh g⁻¹, or 0.03 to 0.02 mAh cm⁻² in area) over 1000 charge/discharge cycles at 0.5 mA cm⁻². Moreover, the high voltage efficiency could also be attributed to the iodine cathode prepared through an in situ absorption technique. When the I₃⁻ concentration was increased from 1.0 to 2.0 M, the 2-1/1 CEMA Zn-I batteries delivered an initial specific capacity of 127 mAh g⁻¹ (or 0.06 mAh cm⁻² in area) and a capacity retention ratio of 65.7% (83 mAh g⁻¹ or 0.04 mAh cm⁻² in area) after 1000 cycles at 0.5 mA g⁻¹ Figure 4d. Further increasing the I₃⁻ concentrations to 10 M, the 10-1/1 CEMA Zn-I batteries delivered a specific capacity of 36 mAh g⁻¹ (or 0.05 mAh cm⁻² in area) at 5.0 mA cm⁻², as presented in Figure 4e. The slight capacity decay may be partially attributed to the consumption of (OTf)⁻ ions through chemical reactions with the Zn anode beneath the less dense interfacial layer. These electrochemical results suggested that the CEMA Zn-I batteries could be cycled over 1000 times with a high coulombic efficiency approaching 100%, by utilizing the oxidative ability of (OTf)⁻ toward triiodide species to form insoluble iodine sediment particles. However, a critical concentration of I₃⁻ exists, beyond which the redox reactions

of largely loaded I₃⁻ species are limited, thereby reducing the charge cutoff voltage and/or requiring greater current densities to suppress the unwanted HER. For example, compared to the 1-1/1 and 2-1/1 CEMA Zn-I batteries operated at 0.5 mA cm⁻² under a charge cutoff voltage of 1.4 V vs Zn/Zn²⁺, the 10-1/1 counterpart operated at 5.0 mA cm⁻² under a suppressed charge cutoff voltage of 1.27 V vs Zn/Zn²⁺ (Figure S11, Supporting Information), resulting in a relatively lower capacity of 105 mAh g⁻¹. Therefore, to achieve optimal capacity values, the concentration of triiodide species needs to be controlled while modulating the charge cutoff voltage and/or working current density.

The feasibility of the proposed CEMA Zn-I batteries was further evaluated under a more rigorous test setup using pouch-type batteries, showing the suppression of swelling due to the HER. A set of 4-1/1 CEMA Zn-I batteries was produced and powered a LED lamp, as demonstrated in Figure 5a. During galvanostatic charge/discharge cycling tests, the pouch-type CEMA Zn-I batteries exhibited consistent voltage profiles and a stable specific capacity of 96 mAh g⁻¹ (or 0.10 mAh cm⁻² in area) at 2.5 mA cm⁻², with a high coulombic efficiency of 99.2% (Figure 5b,c). Furthermore, the pouch-type batteries maintained their original thickness after cycling, without any observable swelling. The

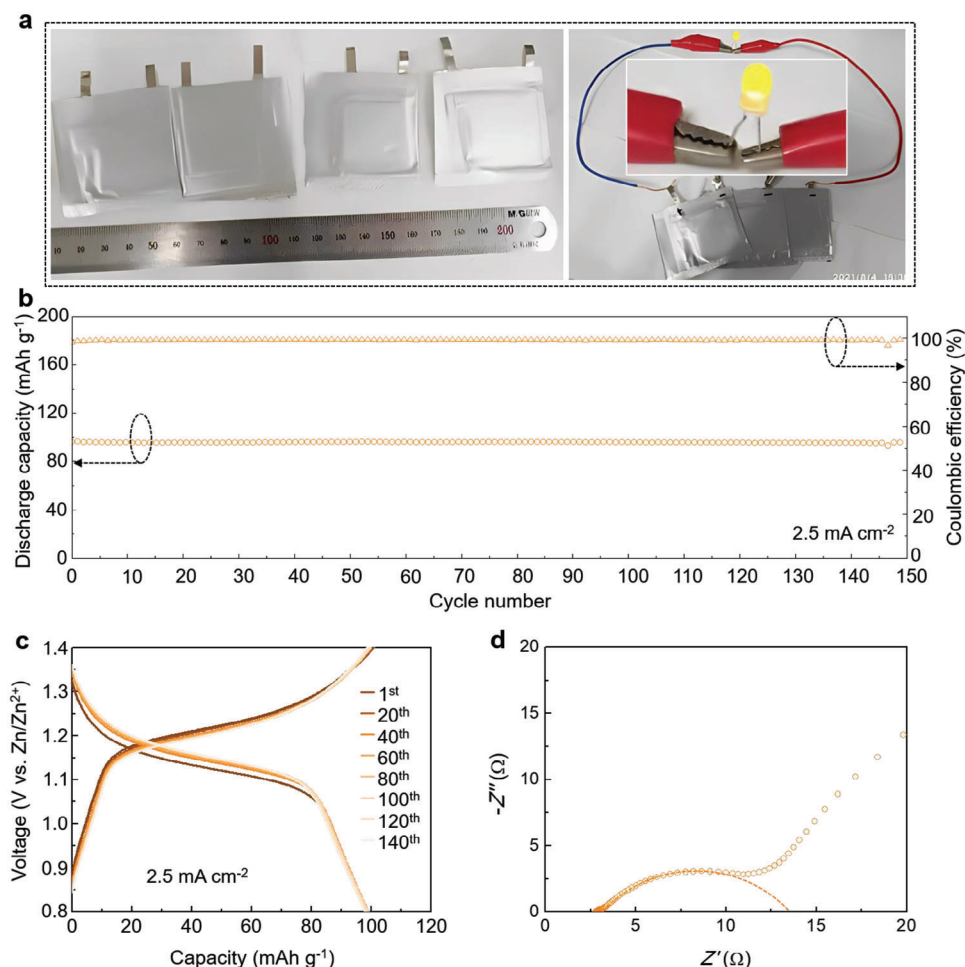


Figure 5. Electrochemical performance of pouch-type CEMA Zn-I batteries. a) Photographs of the as-fabricated pouch-type CEMA Zn-I batteries powering a LED lamp. b) Cycling tests, c) representative voltage profiles, and d) EIS curve of the pouch-type CEMA Zn-I batteries.

electrochemical impedance spectroscopy (EIS) of the pouch-type CEMA Zn-I batteries revealed a charge-transfer impedance of $\approx 10 \Omega$, as depicted in Figure 5d. These experimental findings indicate that the electrode/electrolyte mutualistic strategy is efficient in constructing aqueous Zn-I batteries, which exhibit retarded HER and iodide redox reaction-dominated charge storage during battery operation.

3. Conclusion

In this study, we demonstrate the oxidative effect of (OTf)⁻ on iodide and triiodide species and utilize this effect to fabricate a novel type of CEM mixture for CEMA Zn-I batteries. By exploiting the CEM mixture, we were able to produce an iodine host cathode and aqueous electrolyte through a facile in situ filtration process. During battery operation, we explored the competitive effects of the iodide redox and the HER processes in terms of I_2/I^- ratio and I_3^- concentration. Severe ionization within the electrolyte would lower the critical potential for HER and facilitate its aggravation. However, by optimizing the I_2/I^- ratio and I_3^- concentration, we were able to achieve long-term cycling capability and high-rate performance with well-suppressed HER.

Our findings suggest that the CEMA Zn-I batteries constructed based on the oxidation effects of (OTf)⁻ on iodide species represent a promising strategy for advancing portable and low-cost aqueous Zn-I batteries.

Supporting Information

Supporting Information is available from the Wiley Online Library or from the author.

Acknowledgements

The authors appreciate the financial support from the National Natural Science Foundation of China (Nos. 22022505 and 22109069), the Fundamental Research Funds for the Central Universities of China (Nos. 020514380266, 020514380272, and 020514380274), the Scientific and Technological Innovation Special Fund for Carbon Peak and Carbon Neutrality of Jiangsu Province (No. BK20220008), the Scientific and Technological Achievements Transformation Special Fund of Jiangsu Province (No. BA2023037), the Natural Science Foundation of Jiangsu Province (BK20221446), the Doctoral Innovation and Entrepreneurship Program of Jiangsu Province (JSSCBS20210045), the International Collaboration Research Program of Nanjing City (Nos. 202201007 and 2022SX00000955),

and the Gusu Leading Talent Program of Scientific and Technological Innovation and Entrepreneurship of Wujiang District in Suzhou City (No. ZXL2021273).

Conflict of Interest

The authors declare no conflict of interest.

Data Availability Statement

The data that support the findings of this study are available from the corresponding author upon reasonable request.

Keywords

aqueous batteries, chemical oxidation effects, electrochemistry, precipitated iodine electrodes

Received: September 22, 2023

Revised: November 4, 2023

Published online:

- [1] F. Wang, O. Borodin, T. Gao, X. Fan, W. Sun, F. Han, A. Faraone, J. A. Dura, K. Xu, C. Wang, *Nat. Mater.* **2018**, 17, 543.
- [2] T. Zhang, Y. Tang, G. Fang, C. Zhang, H. Zhang, X. Guo, X. Cao, J. Zhou, A. Pan, S. Liang, *Adv. Funct. Mater.* **2020**, 30, 2002711.
- [3] S. Chen, Q. Chen, J. Ma, J. Wang, K. S. Hui, J. Zhang, *Small* **2022**, 18, 2200168.
- [4] P.-F. Zhang, Z. Wu, S.-J. Zhang, L.-Y. Liu, Y. Tian, Y. Dou, Z. Lin, S. Zhang, *Nano Energy* **2022**, 102, 107721.
- [5] S. J. Zhang, J. Hao, Y. Zhu, H. Li, Z. Lin, S. Z. Qiao, *Angew. Chem., Int. Ed.* **2023**, 135, e202301570.
- [6] Y. Yang, J. Xiao, J. Cai, G. Wang, W. Du, Y. Zhang, X. Lu, C. C. Li, *Adv. Funct. Mater.* **2021**, 31, 2005092.
- [7] B. Wang, J. Yan, Y. Zhang, M. Ye, Y. Yang, C. C. Li, *Adv. Funct. Mater.* **2021**, 31, 2102827.
- [8] Y. Yang, H. Hua, Z. Lv, W. Meng, M. Zhang, H. Li, P. Lin, J. Yang, G. Chen, Y. Kang, Z. Wen, J. Zhao, C. C. Li, *ACS Energy Lett.* **2023**, 8, 1959.
- [9] M. Zhang, H. Hua, P. Dai, Z. He, L. Han, P. Tang, J. Yang, P. Lin, Y. Zhang, D. Zhan, J. Chen, Y. Qiao, C. C. Li, J. Zhao, Y. Yang, *Adv. Mater.* **2023**, 35, 2208630.
- [10] H. Liu, C.-Y. Chen, H. Yang, Y. Wang, L. Zou, Y.-S. Wei, J. Jiang, J. Guo, W. Shi, Q. Xu, P. Cheng, *Adv. Mater.* **2020**, 32, 2004553.
- [11] F. Yu, L. Pang, X. Wang, E. R. Wacławik, F. Wang, K. Ostrikov, H. Wang, *Energy Storage Mater.* **2019**, 19, 56.
- [12] Y. Kang, G. Chen, H. Hua, M. Zhang, J. Yang, P. Lin, H. Yang, Z. Lv, Q. Wu, J. Zhao, Y. Yang, *Angew. Chem., Int. Ed.* **2023**, 62, e202300418.
- [13] K. W. Leong, Y. Wang, M. Ni, W. Pan, S. Luo, D. Y. C. Leung, *Renewable Sustainable Energy Rev.* **2022**, 154, 111771.
- [14] C.-X. Zhao, L. Yu, J.-N. Liu, J. Wang, N. Yao, X.-Y. Li, X. Chen, B.-Q. Li, Q. Zhang, *Angew. Chem., Int. Ed.* **2022**, 134, e202208042.
- [15] A. Amiri, R. Sellers, M. Naraghi, A. A. Polycarpou, *ACS Nano* **2023**, 17, 1217.
- [16] G. Chang, J. Liu, Y. Hao, C. Huang, Y. Yang, Y. Qian, X. Chen, Q. Tang, A. Hu, *Chem. Eng. J.* **2023**, 457, 141083.
- [17] Y. Yuan, R. Sharpe, K. He, C. Li, M. T. Saray, T. Liu, W. Yao, M. Cheng, H. Jin, S. Wang, K. Amine, R. Shahbazian-Yassar, M. S. Islam, J. Lu, *Nat. Sustainability* **2022**, 5, 890.
- [18] Z. Shen, Y. Liu, L. Luo, J. Pu, Y. Ji, J. Xie, L. Li, C. Li, Y. Yao, G. Hong, *Small* **2022**, 18, 2204683.
- [19] H. X. Dang, A. J. Sellathurai, D. P. J. Barz, *Energy Storage Mater.* **2023**, 55, 680.
- [20] L. Yan, S. Zhang, Q. Kang, X. Meng, Z. Li, T. Liu, T. Ma, Z. Lin, *Energy Storage Mater.* **2023**, 54, 339.
- [21] M. Liu, Q. Chen, X. Cao, D. Tan, J. Ma, J. Zhang, *J. Am. Chem. Soc.* **2022**, 144, 21683.
- [22] Q. Guo, H. Wang, X. Sun, Y. Yang, N. Chen, L. Qu, *ACS Mater. Lett.* **2022**, 4, 1872.
- [23] Y. Yang, S. Liang, B. Lu, J. Zhou, *Energy Environ. Sci.* **2022**, 15, 1192.
- [24] W. Shang, J. Zhu, Y. Liu, L. Kang, S. Liu, B. Huang, J. Song, X. Li, F. Jiang, W. Du, Y. Gao, H. Luo, *ACS Appl. Mater. Interfaces* **2021**, 13, 24756.
- [25] D. Lin, D. Rao, S. Chiovoloni, S. Wang, J. Q. Lu, Y. Li, *Nano Lett.* **2021**, 21, 4129.
- [26] M. Xing, Z. Z. Zhao, Y. J. Zhang, J. W. Zhao, G. L. Cui, J. H. Dai, *Mater. Today Energy* **2020**, 18, 100534.
- [27] S. Yang, X. Guo, H. Lv, C. Han, A. Chen, Z. Tang, X. Li, C. Zhi, H. Li, *ACS Nano* **2022**, 16, 13554.
- [28] Y. Yang, S. Liang, J. Zhou, *Curr. Opin. Electrochem.* **2021**, 30, 100761.
- [29] L. Ma, Q. Li, Y. Ying, F. Ma, S. Chen, Y. Li, H. Huang, C. Zhi, *Adv. Mater.* **2021**, 33, 2007406.
- [30] L. Hong, L.-Y. Wang, Y. Wang, X. Wu, W. Huang, Y. Zhou, K.-X. Wang, J.-S. Chen, *Adv. Sci.* **2022**, 9, 2104866.
- [31] J. Yang, B. Yin, Y. Sun, H. Pan, W. Sun, B. Jia, S. Zhang, T. Ma, *Nano-Micro Lett.* **2022**, 14, 42.
- [32] C. Li, X. Xie, S. Liang, J. Zhou, *Energy Environ. Mater.* **2020**, 3, 146.
- [33] A. Bayaguud, Y. Fu, C. Zhu, *J. Energy Chem.* **2022**, 64, 246.
- [34] N. Wang, Y. Yang, X. Qiu, X. Dong, Y. Wang, Y. Xia, *ChemSusChem* **2020**, 13, 5556.
- [35] H. Yang, Y. Qiao, Z. Chang, H. Deng, P. He, H. Zhou, *Adv. Mater.* **2020**, 32, 2004240.
- [36] K. K. Sonigara, J. Zhao, H. K. Machhi, G. Cui, S. S. Soni, *Adv. Energy Mater.* **2020**, 10, 2001997.
- [37] W. Wu, C. Li, Z. Wang, H.-Y. Shi, Y. Song, X.-X. Liu, X. Sun, *Chem. Eng. J.* **2022**, 428, 131283.
- [38] Z. Li, X. Wu, X. Yu, S. Zhou, Y. Qiao, H. Zhou, S.-G. Sun, *Nano Lett.* **2022**, 22, 2538.
- [39] P. Prabakaran, R. P. Manimuthu, *Ionics* **2016**, 22, 827.
- [40] R. Perveen, S. Haque Inamuddin, A. Nasar, A. M. Asiri, G. M. Ashraf, *Sci. Rep.* **2017**, 7, 13353.
- [41] J.-K. Wu, M.-J. Yin, W. Han, N. Wang, Q.-F. An, *J. Mater. Sci.* **2020**, 55, 12607.
- [42] A. Bentsis, A. Boukhriess, A. M. Grancaric, M. E. Bouchti, M. E. Achaby, S. Gmouh, *Cellulose* **2019**, 26, 2139.
- [43] C. Song, Z. Gong, C. Bai, F. Cai, Z. Yuan, X. Liu, *Nano Res.* **2022**, 15, 3170.
- [44] S. Chai, J. Yao, Y. Wang, J. Zhu, J. Jiang, *Chem. Eng. J.* **2022**, 439, 135676.
- [45] W. Li, K. Wang, K. Jiang, *J. Mater. Chem. A* **2020**, 8, 3785.
- [46] Y. Wu, Z. Zhu, D. Shen, L. Chen, T. Song, T. Kang, Z. Tong, Y. Tang, H. Wang, C. S. Lee, *Energy Storage Mater.* **2022**, 45, 1084.
- [47] V. Sharma, S. Basak, K. Rishabh, H. Umair, S. W. Ali, *Cellulose* **2018**, 25, 6191.
- [48] Y. Yang, C. Liu, Z. Lv, H. Yang, Y. Zhang, M. Ye, L. Chen, J. Zhao, C. C. Li, *Adv. Mater.* **2021**, 33, 2007388.
- [49] Y. Yang, C. Liu, Z. Lv, H. Yang, X. Cheng, S. Zhang, M. Ye, Y. Zhang, L. Chen, J. Zhao, C. C. Li, *Energy Storage Mater.* **2021**, 41, 230.
- [50] L. Wei, P. Wang, Y. Yang, R. Luo, J. Li, X. Gu, Z. Zhan, Y. Dong, W. Song, R. Fan, *J. Nanopart. Res.* **2018**, 20, 110.